Vacuum Ultraviolet Spectral Measurements for Superorbital Earth Entry in the X2 Expansion Tube

Umar A. Sheikh [1], Richard G. Morgan [2] and Timothy J. McIntyre [3]
The University of Queensland, QLD, 4072

Experiments were conducted using the X2 expansion tube at two conditions representative of flight velocities of $10.0\,\mathrm{km/s}$ and $12.2\,\mathrm{km/s}$ for a vehicle entry into Earth's atmosphere. Calibrated spectral measurements were made of radiating shock layers across and through the surface of a model. These measurements provide a unique dataset for the validation of computational codes used in the calculation of incident VUV radiative heat flux. Computational simulations at equilibrium gas chemistry were conducted using the Specair program and showed good agreement with the measurements.

---

[1] Post-Doctoral Research Fellow, The Centre for Hypersonics, School of Mechanical and Mining Engineering, now at Centre de Recherches en Physique des Plasmas, Ecole Polytechnique Federal de Lausanne, Switzerland, `umar.sheikh@epfl.ch`

[2] Director of the Centre for Hypersonics, School of Mechanical and Mining Engineering, `r.morgan@uq.edu.au`

[3] Associate Professor, School of Mathematics and Physics, `t.mcintyre@uq.edu.au`

Nomenclature

A_p = Aperture

A_{IN} = Inlet Area

A_{OUT} = Outlet Area

C = Circle of Confusion / Concentration / Conductance

CCD = Charge Coupled Device

Δ = Shock Stand Off

$\dot{m}$ = Mass Flow Rate

f = Focal Length

F_N = F-number

H_o = Total enthalpy

h_s = Sensible enthalpy

I = Integrated Spectral Radiance / Signal Intensity

$ICCD$ = Intensified Charge Coupled Device

λ = Wavelength

ρ = Density

s = Optical Path Length

t = Time

U = Velocity

VUV = Vacuum Ultraviolet

x = Length of Model

y = Height of Model

$'$ = Post Shock Properties

I. Introduction

A major design challenge for re-entry capsules lies in the modelling of convective and radiative heat transfer to the surface of a vehicle, and the vacuum ultraviolet (VUV) spectral range contributes a significant portion of the total radiative heat flux. The VUV spectral range is also responsible for the largest uncertainties and this is predominantly due to the lack of available experimental data, leading to large safety factors in the design of thermal protection systems [1]. At some high velocity points on superorbital re-entry trajectory, over 50% of the total heat flux can be radiative, principally from the vacuum ultraviolet (VUV) spectral range between 100 nm and 200 nm [2]. To reduce the associated uncertainties in the design of thermal protection systems, it is necessary to better understand the physical processes behind radiative heat transfer at these wavelengths.

Whilst radiative heating for hypersonic craft has been an area for significant research for over 60 years, there is minimal experimental data available in the VUV spectral range. One of the reasons behind this lack of data is the additional complexity involved in measuring VUV radiation. High vacuum systems are required to remove molecular oxygen and water vapour from the optical path to allow for transmission of VUV radiation. Standard optical components do not transmit at these wavelengths and therefore specialised crystals such as magnesium fluoride and calcium fluoride are required.

A study of 15 facilities employed to obtain spectral measurements in radiating flow fields, representative of re-entry shock layers, revealed that only four facilities are currently capable of measuring radiation in the VUV: the shock tunnels at NASA and JAXA, the X2 expansion tube at the University of Queensland and the inductively coupled plasma torch at Ecole Centrale Paris, as shown in Table 1 [3-22]. The arc-jet at NASA was used in 1997 to obtain measurements in the VUV through the surface of a helium cooled model [3]. However this system was only calibrated to within a factor of two and the free stream gas was altered too severely in the arc-jet to be representative of free stream flow experienced in flight. The flow of helium also disabled the formation of a boundary layer and disrupted the shock layer significantly.

All of the facilities currently capable of measuring VUV spectra, other than the X2 expansion tube, observe a shock wave or slug of radiating gas as it passes across a viewing port in standard

Table 1 Emission spectroscopy capabilities of various facilities around.

Wavelength Range (nm)	VUV <200	UV 200-390	VIS 390-700	NIR 700-1100	IR >1100
Shock Tunnels and Expansion Tubes					
EAST [4, 5]	x	x	x	x	x
HVST [6]	x	x	x	x	
X2 [7–9]	x	x	x	x	
X3 [7]		x	x	x	
LENS XX [10]		x	x	x	
Plasma Wind Tunnels and ARC Jets					
NASA ARC [3, 11]	x	x	x	x	
Scirocco [12, 13]		x	x	x	
Plasmatron [13, 14]		x	x	x	
DLR L3K [13, 15]		x	x	x	
IRS PWK [16]		x	x	x	
Onera F4 [13, 17]		x	x	x	
Plasma Torches					
EM2C ICP [18, 19]	x	x	x	x	x
PHEDRA [13, 20, 21]		x	x	x	
Ballistic Ranges					
HFFGAF [13, 22]		x	x	x	

operating mode. This does not allow for a model to be placed in the flow and radiation to be measured through a boundary layer, restricting observations to across the shock layer. Consequently, the radiation measured as the shock wave or radiating gas crosses the field of view is used to validate computational programs and the data extrapolated to calculate incident radiation. The aim of this study was to produce a set of measurements observing radiation across a shock layer and compare it with the radiation measured through the surface of the model. This unique data set will enable

investigation into the validity of current methods used to predict incident radiative heat flux to the surface of a vehicle in the VUV spectral range.

II.   Facility Description

The X2 facility at The University of Queensland is a free piston, compressed gas driven expansion tube capable of producing flows with enthalpies in excess of $75\,\mathrm{MJ/kg}$ for test times in excess of $100\,\mu\mathrm{s}$. A range of configurations is possible for this facility, such as the use of detachable nozzles, additional driver sections and a range of orifice plates to vary the internal diameter at the primary diaphragm. For this study, a single driver tube with a $208\,\mathrm{mm}$ nozzle configuration as shown in Figure 1 was used. A full description of the facility is available in Gildfind et al. [23].
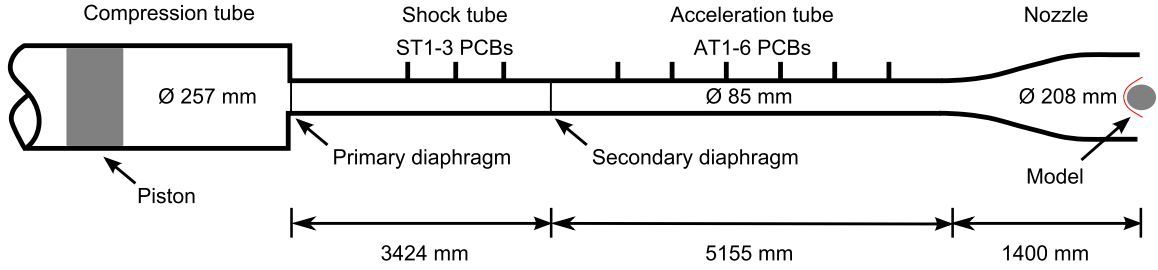

Fig. 1 Schematic of the X2 expansion tube configuration used for this study. ST1-3 and AT1-6 PCBs are the shock tube and acceleration tube pressure transducers.

A.   Operating Conditions

Two conditions with free stream velocities of $9.7\,\mathrm{km/s}$ and $11.9\,\mathrm{km/s}$ were produced for this study and are outlined in Table 2. Previous experimental data and basic shock wave relations, as outlined in Gildfind [24], were utilised to compute the fill pressures required. These estimates were tested by the numerical simulation code *Pitot*[25] to calculate flow conditions at equilibrium chemistry using the CEA look up tables [26].

The free stream conditions produced in the expansion tube are of significantly higher temperatures than those experienced in flight. The increased temperatures result in a portion of the free stream energy being stored as sensible enthalpy (h_s). To match post shock flight temperatures, the total enthalpy, H_o, must be equivalent at ground testing free stream conditions. This equivalencey

Table 2 Free stream test conditions calculated using *Pitot* and available measured values.

Condition 1		
Parameter	Calculated	Measured
Primary shock velocity (km/s)	4.76	4.70 $\pm$0.12
Secondary shock velocity (km/s)	9.57	9.60 $\pm$0.30
Static pressure at nozzle entry (Pa)	4,710	5,000 $\pm$750
Pitot pressure (kPa)	115	115 $\pm$12
Test gas velocity (km/s)	9.71	N/A
Test gas temperature (K)	2,500	N/A
Test gas Mach number	10.6	N/A
Test gas density (kg/m^3)	1.26$\times 10^{-3}$	N/A
Test gas enthalpy (MJ/kg)	50.3	N/A
Test gas static pressure (Pa)	930	N/A

Condition 2		
Parameter	Calculated	Measured
Primary shock velocity (km/s)	5.64	5.70 $\pm$0.15
Secondary shock velocity (km/s)	11.7	11.50 $\pm$0.40
Static pressure at nozzle entry (Pa)	4,460	7,000 $\pm$1800
Pitot pressure (kPa)	135	140 $\pm$28
Test gas velocity (km/s)	11.8	N/A
Test gas temperature (K)	2,800	N/A
Test gas Mach number	11.9	N/A
Test gas density (kg/m^3)	1.00$\times 10^{-3}$	N/A
Test gas enthalpy (MJ/kg)	74.5	N/A
Test gas static pressure (Pa)	870	N/A

allows for a correlation between expansion tube free stream velocity, U_∞, and flight equivalent velocity, U_e.

$$H_o = h_s + \frac{U_\infty^2}{2} = \frac{U_e^2}{2} \tag{1}$$

Using this energy balance, the conditions produced for this study match high radiative heating points on a Lunar return and a Mars return trajectory with $10.0\,\mathrm{km/s}$ and $12.2\,\mathrm{km/s}$ flight equivalent velocities.

To validate the calculated free stream values from *Pitot*, the primary shock wave velocity, secondary shock wave velocity, static pressure at the inlet of the nozzle and pitot pressure measured at the exit of the nozzle were compared with experimental values. Pitot pressures were obtained in the test section using an array of 15 degree conical glancing impact pressure probes in a rake formation, as shown in Figure 2 [24]. Using the rake formation, it was possible to measure a radial distribution of the pitot pressures and ensure the core flow produced was large enough to house the entire model. Detailed design and testing of the conical pressure probes is outlined in Gildfind [24]. The results of the *Pitot* calculations and comparisons with experimental measurements are shown in Table 2.
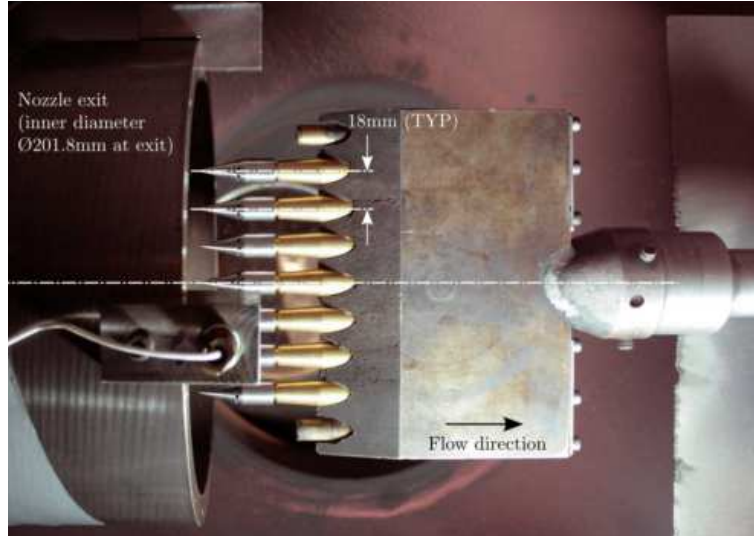

Fig. 2 Pitot rake arrangement with conical glancing pressure probes for conditions testing.

The primary shock wave velocity, secondary shock wave velocity and pitot pressure measured at the exit of the nozzle were in good agreement with the calculated values as shown in Table 2. The static pressure at the entry of the nozzle was also in good agreement for Condition 1 but lay

just outside the bounds of uncertainty for Condition 2. The cause of this discrepancy is currently being investigated.

The temporal resolution of the pitot probes allowed for an estimate of the steady test time achieved by the conditions. An indicator of steady test time is time between the arrival of the test gas until the arrival of the higher pressure under-expanded gas. Figure 3 presents the measured pitot pressure values at both conditions. From these results, test times of $150\,\mu s$ and $100\,\mu s$ were estimated for Conditions 1 and 2 respectively.
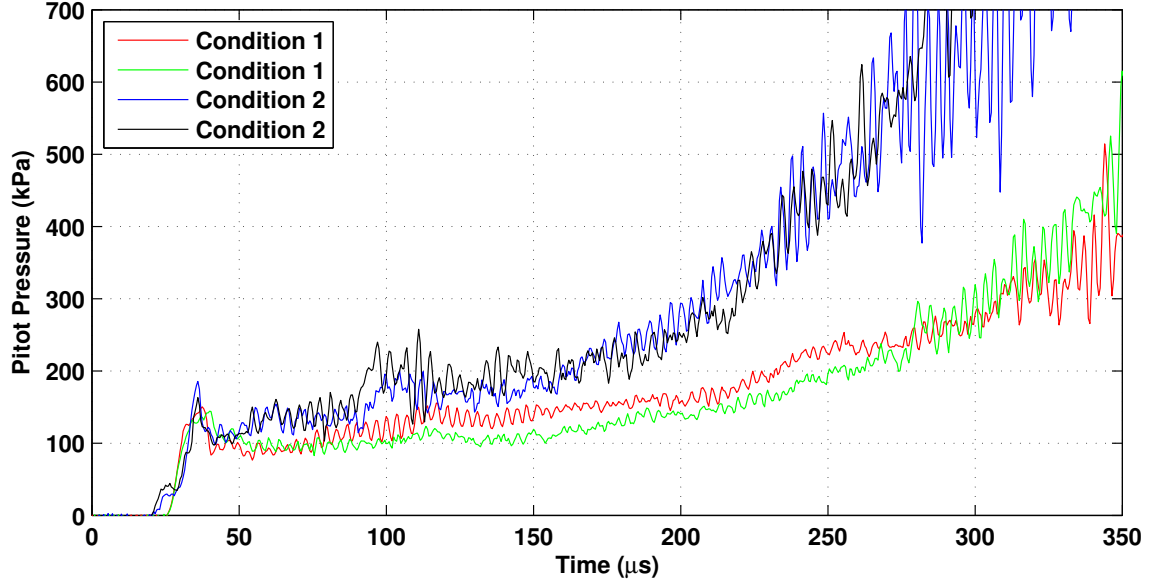
Fig. 3 Average core flow pitot pressures measured for two shots at both conditions. Estimated test time for Condition 1 is $50\,\mu s$ to $200\,\mu s$ and estimated test time for Condition 2 is $50\,\mu s$ to $150\,\mu s$.

III. Experiment Design

A simple two dimensional blunt model was used to reduce computational complexities in simulating the model, produce a large shock stand off, drive flows closer to equilibrium, and allow for the use of flat windows without disruption to the surface shape of the model. Consequently it had a simple configuration of a $25\,mm$ tall, $90\,mm$ long rectangular bar. The height of the model was the minimum possible to house available stock size magnesium fluoride windows and the length of the model was set to utilise the entire core flow available. The aspect ratio produced by this shape

was 3.6.

An estimate of the shock stand off is necessary to select the desired optical magnification of the focussing system. Literature describing the variation of three-dimensional shock stand off as a function of aspect ratio is available for blunt cylindrical shapes [27] however none was found for a flat faced model. A first order approximation was carried out using a simplified three-dimensional shock layer region and the conservation of mass principle. The approximately planar nature of the shock wave over the model allowed for the shock region to be modelled as a rectangular shock layer, as shown in Figure 4.
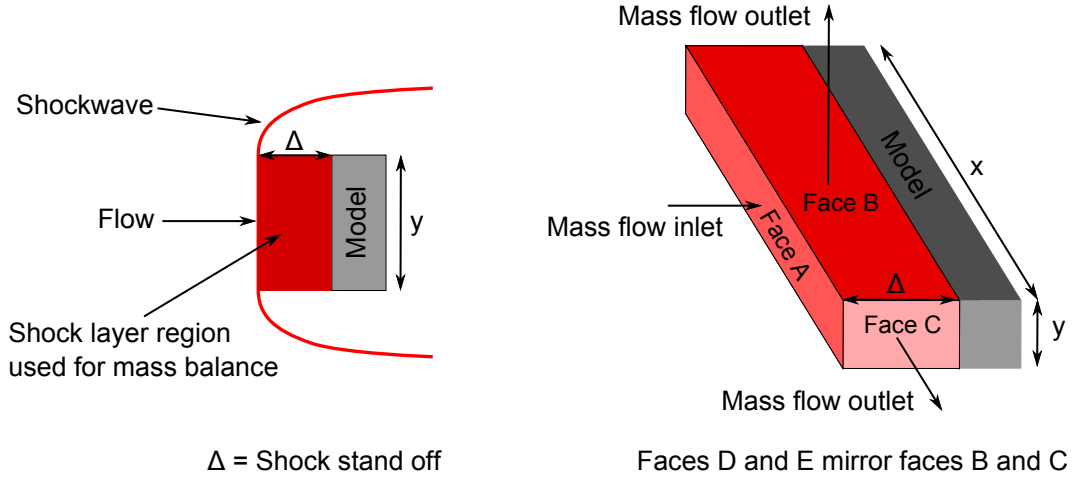
Fig. 4 Left - Side on view of idealised two-dimensional shock stand off. Right - Three dimensional view of idealised region used for mass flow balance.

The shock stand off, Δ, can be estimated by equating the mass flow into the shock layer through face A, and out of the shock layer through faces B to E, noting that the model acts as a boundary to the flow.

$$\dot{m}_{IN} = \rho U A_{Face\,A} \; = \; \dot{m}_{OUT} = \rho' U' A_{Faces\,B\,to\,E} \tag{2}$$

where ρ' and U' are the post shock density and velocity. Substituting $A_{Face\,A} \; = \; x\,y$ and $A_{Faces\,B\,to\,E} = 2(x\Delta + y\,\Delta)$, the shock stand off relationship equates to

$$\Delta_{3D} \;\; = \;\; \frac{\rho U\,x\,y}{\rho' U'\,2\,(x+y)} \tag{3}$$

9

In the 2D case, x>>y and therefore x+y can be approximated to x, giving

$$\Delta_{2D} \;=\; \frac{\rho U \, x \, y}{\rho' U' \, 2 \, x} \tag{4}$$

Taking the ratio of the two shock stand off estimates gives

$$\frac{\Delta_{3D}}{\Delta_{2D}} \;=\; \frac{\rho U \, x \, y}{\rho' U' \, 2 \, (x + y)} \frac{\rho' U' \, 2 \, x}{\rho U \, x \, y} \tag{5}$$

$$\frac{\Delta_{3D}}{\Delta_{2D}} \;=\; \frac{x}{x + y} \tag{6}$$

By substituting the aspect ratio, AR, the relationship can be further simplified

$$substituting \; AR \;=\; \frac{x}{y} \tag{7}$$

$$\frac{\Delta_{3D}}{\Delta_{2D}} \;=\; \frac{AR}{AR + 1} \tag{8}$$

A plot of this relationship is shown in Figure 5 for aspect ratios between 0.1 and 20. The aspect ratio produced by the model used in this study is 3.6 and was predicted to create a shock stand off that is 76% of the idealised two-dimensional value. Based on preliminary simulations, this reduced shock stand off is expected to still be greater than the length scale required to reach equilibrium chemistry for both conditions.
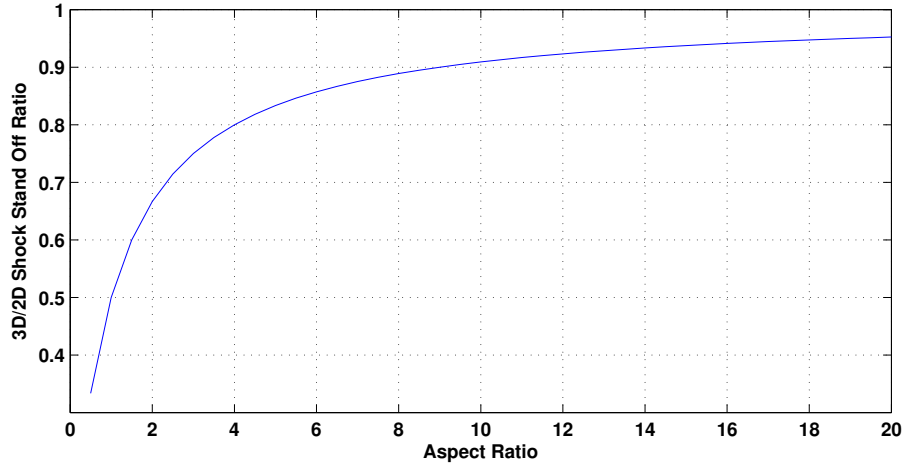

Fig. 5 First order approximation of shock stand off correction for varying aspect ratio square bodies in supersonic and hypersonic flow.

A.   Through Surface Spectral Measurements

Experiments have previously attempted to measure radiation incident of the surface of the model through the use of helium cooled windows or optical fibres embedded in the surface of a model with limited success [3, 28]. The use of helium to actively cool the front face of the window produced disruptions in the boundary layer and consequently resulted in a shock layer that was not representative of one experienced in flight. Experiments carried out to investigate the possibility of using optical fibres embedded in the surface of a model were unsuccessful due to the high temperature shock layer causing the cladding to ablate and altering the properties of the fibre. An approach of this type was considered for this study however the signal losses through an optical fibre in the VUV spectral range ruled out their applicability at the shorter wavelengths of interest.

An operational advantage of using a pulsed facility such as X2 is that test times are in the order of hundreds of microseconds and thus models do not require active cooling. This enables a simpler design of the model and negates the need for cooling gases that could interfere with the shock layer. Magnesium fluoride was selected as the material for the windows as it provided the best thermal and optical properties across the spectral range of interest [29]. Based on the thermal expansion coefficients and material strength properties, it was calculated that the windows could withstand the high temperatures during the test time but it was expected that the unsteady flow and driver gas arrival after the test time could heat the windows enough to damage the surface finish and influence the transmission properties. Observations made with a high speed imaging camera during an X2 experiment were conducted to validate these calculations and it was found that all windows maintained structural integrity during the test time [30]. The subsequent arrival of the under expanded test gas and driver gas region caused significant structural damage to the windows which consequently had to be replaced after each test.

The optical system was designed to take radiation incident on the model to an external detection system through the use of a mirror installed in a high vacuum housing behind the model and an evacuated light tube, as shown in Figure 6. The model was positioned 150 mm upstream from the mirror housing assembly to ensure there would be no interference from shock waves forming over the housing and connected through an evacuated light tube. Pitot and static pressure probes were

11

installed on the top of the mirror housing, out of the plane of the model, for additional diagnostic capabilities.
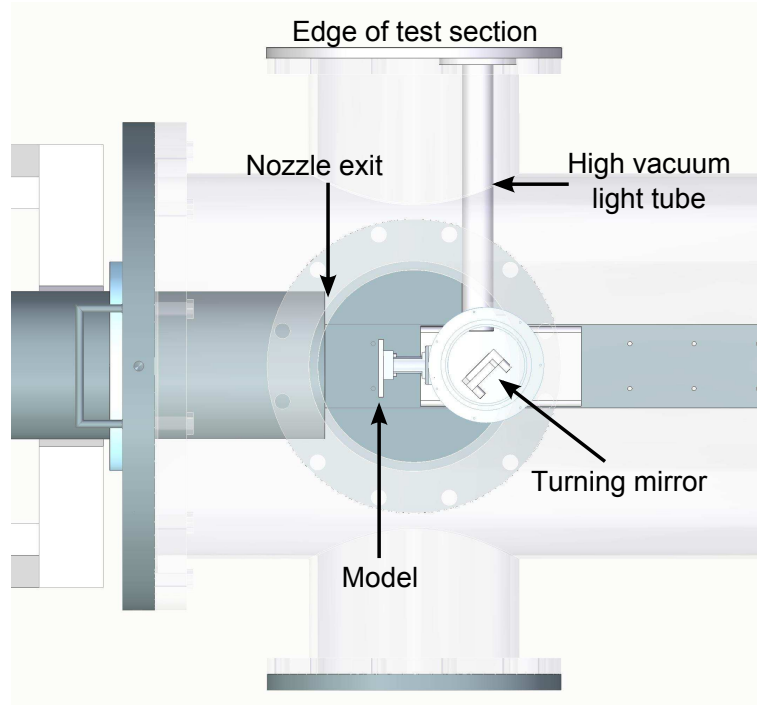

Fig. 6 Top down view of high vacuum path to model with mirror housing assembly and pressure probes.

B.   Across Surface Spectral Measurements

Measurements were also conducted to observe radiation across the surface from side on to the flow, as generally conducted in other radiation experiments. A particular concern for these measurements is absorption by molecular oxygen in the test section outside the core flow. To eliminate this absorption, an evacuated light tube was employed. The light tube was sealed by a 'fence' housing a magnesium fluoride window 10 mm from the model. The role of the fence was to produce an acute angled shock wave that would dissociate the molecular oxygen in the core flow directly in front of the viewing window whilst ensuring the disruption was small enough not to affect the shock layer formed over the model. An annotated image of the arrangement during testing is shown in Figure 7. The Lu et al. [31] absorption cross-sections for molecular oxygen were used to calculated the absorption in the 10 mm gap between the window and the model. The level of

absorption was found to be less than 2% due to the small size of the gap, relatively low pressure of the free stream gas and the partially dissociated state of oxygen within the test gas.
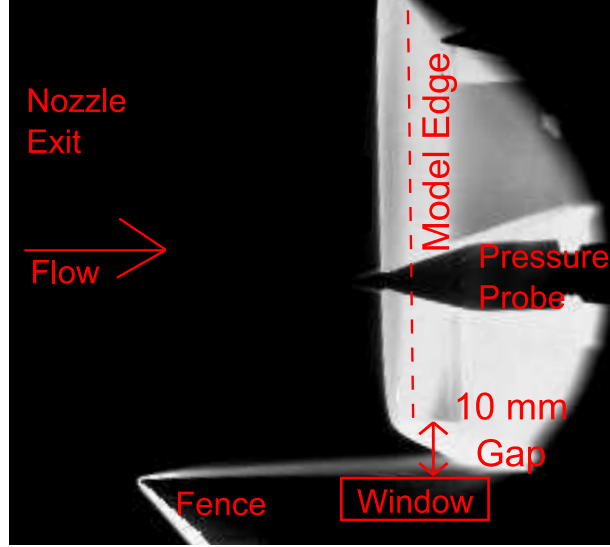

Fig. 7 Annotated top down image acquired during the test time illustrating the shock wave created by the fence not interacting with the shock layer around the model. The observational window position is centred upstream of the surface of the model at a distance of 10 mm.

C. VUV Emission Spectroscopy System

The spectroscopy system established for this study consisted of a McPherson NOVA 225 normal incidence spectrometer with a focal length of 1.0 m coupled to an Andor iStar generation 2 ICCD with enhanced sensitivity in the VUV spectral range. The iStar generation 2 camera has an 18 mm S20 UV enhanced photocathode utilizing P43 phosphor. The slit width was set to 25 μm for this study and the instrument function was found to be 0.20 nm full width half maximum for the system inferred from the 121.5 nm deuterium lamp spectral line. The sensor of the ICCD consisted of 512 pixels in the spatial direction and 2048 pixels in the wavelength direction. Combined with the dispersion of the grating, a theoretical resolution of 0.06 nm/pixel can be achieved for this spectroscopy system.

A 300 lines/mm grating installed in the system allowed for spectra to be recorded over a 60 nm range in each experiment. The wavelength region selected for this study was 115 nm to 175 nm. Data was initially acquired between 175 nm and 200 nm but has been omitted from this study due

to high levels of iron and carbon contamination in this spectral region. The lower spectral bound of 115 nm was set by the system sensitivity limit.

1. External Focussing Optical System

Two independent optical systems were required to image the radiating shock layer onto the entrance slit of the spectroscopy system. Initial two-dimensional computational simulations predicted shock stand offs of 7.1 mm and 7.4 mm for the two conditions respectively, indicating shock stand offs of approximately 5.4 mm and 5.6 mm for the three-dimensional flow over the model based on the 2D/3D shock stand off correlation calculated. Consequently, the magnification of the optical system was set to image 7.8 mm on the 6.7 mm spatial axis of the ICCD, resulting in approximately 370 pixels imaging the shock layer. A limiting aperture of 10.0 mm was placed on a focussing mirror with a focal length of 500 mm to ensure a depth of field covering the 90 mm model. The circle of confusion was calculated using the relationship found in Pedrotti [32] and found to be 0.35 mm. The depth of field required for through surface measurements was much smaller and therefore a larger aperture of 30.0 mm was utilised to increase the signal strength. The circle of confusion calculated for the through surface optical system was 0.10 mm for a depth of field of 8.5 mm. The final details of both optical systems designed are presented in Table 3 and a schematic shown in Figure 8.

Table 3 Details of optical systems produced.

Optical path	Across surface	Through Surface
Focussing mirror to model centreline (mm)	1088 ±1	1088 ±1
Focussing mirror to slit (mm)	925 ±1	925 ±1
Total optical path (mm)	2013 ±2	2013 ±2
Aperture (mm)	10.0 ±0.3	30.0 ±0.3
F-Number	50.0 ±1.0	16.7 ±0.8
Depth of field (mm)	90.0 ±3.0	8.5 ±1
Calculated circle of confusion (mm)	0.35	0.10
Magnification	0.85	0.85

A high vacuum chamber was designed to house optical components in an environment void of
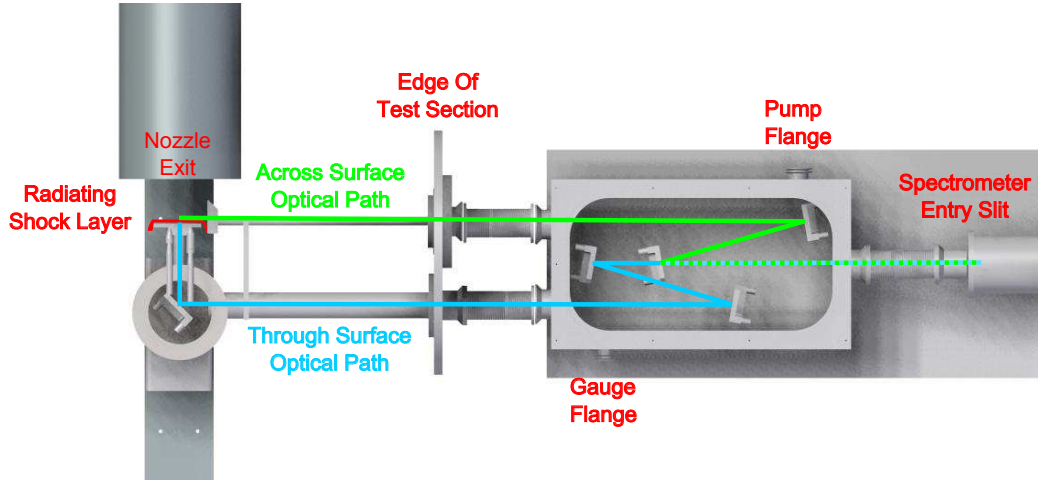
Fig. 8 Imaging optics to observe radiation across and through the surface of the models. Image drawn to scale.

VUV absorbing molecular oxygen and water vapour. To aid the evacuation process, the chamber was designed to have a minimal internal volume and made from 304 grade stainless steel to reduce out gassing [33]. The spectrometer was mounted to align the spatial axis of the spectroscopy system with the stagnation streamline. The spectrometer, optical chamber and test section were coupled with standard vacuum bellows that absorbed any movement of the test section during the experiment.

2. High Vacuum Pressure Requirements

The vacuum pressure required to remove absorption by molecular oxygen and water vapour out gassing from the walls was calculated using the absorption coefficients from Lu [31] for 115 nm to 180 nm in air, Yoshino [34] for the molecular oxygen Schumann-Runge bands between 180 nm and 197 nm and Mota [35] for water vapour between 115 nm and 194 nm. The transmission percentages as a function of wavelength over an optical path of one metre at varying pressures of air and water vapour are presented in Figure 9. It was concluded that pressures in the order of 10^{-4} Torr or 10^{-2} Pascal were required to remove any significant absorption from molecular oxygen in air and any possible absorption through a build up of water vapour from out gassing.
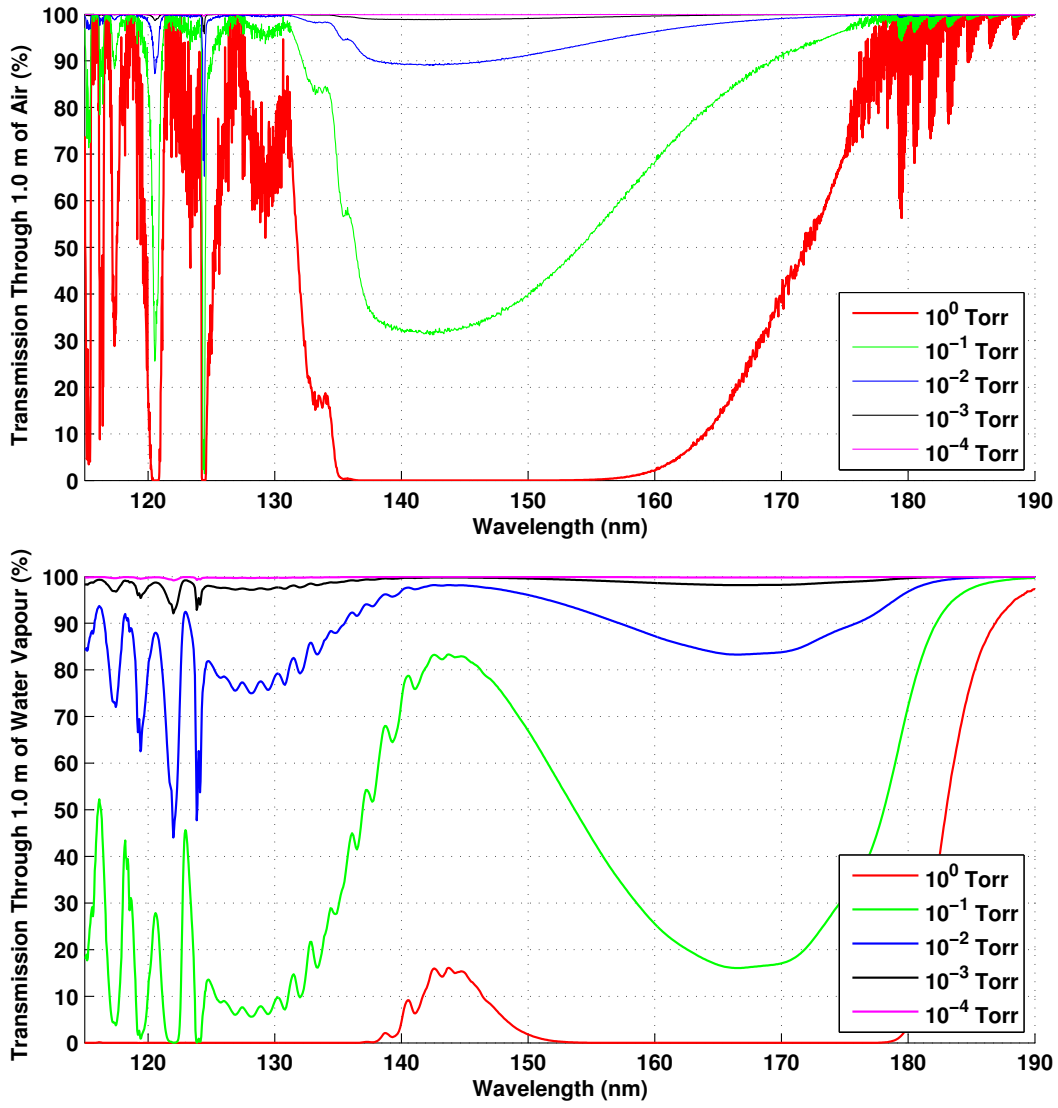
Fig. 9 Transmission percentage of VUV radiation through 1.0 m of air (top) and water vapour (bottom) at varying pressures and room temperature.

3. Calibration

Calibration of the emission spectroscopy system was conducted using a deuterium calibration lamp calibrated at the Physikalisch-Technische Bundesanstalt [36]. The calibration lamp was provided with a known spectral radiance and was used to conduct an in-situ calibration. This approach accounts for any variation in alignment, aperture size, transmission and reflectance of optical elements from the given values as they are all in the optical path during calibration and an experiment.

Care was taken in the alignment of the spot size to ensure the image of the lamp was centred

on the spectrometer slit. Any variation from this position would produce errors in the recorded intensity and consequent calculations of system sensitivity. The system sensitivity as a function of wavelength was calculated by

$$\text{system sensitivity}(\lambda) = \frac{\text{ICCD counts}}{\text{lamp spectral radiance}} \tag{9}$$

The final measured system sensitivity for both optical systems is displayed in Figure 10. The across surface optical system had a comparatively lower sensitivity as they were made with UV focusing mirror, instead of a VUV enhanced mirror. A VUV enhanced focussing mirror was not available at the time of the across surface measurements.
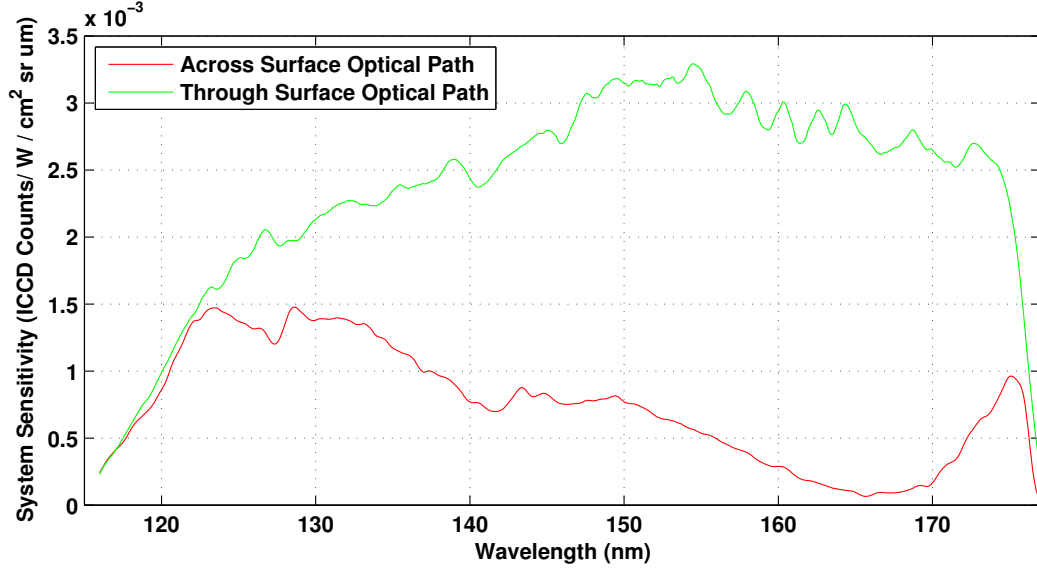

Fig. 10 Final system sensitivity measured for both optical systems.

4. *Spectroscopy System Uncertainty Analysis*

Brandis [37] outlines the five terms most influential in calculating the level of uncertainty in emission spectroscopy are the radius of the aperture, distance to the aperture, the width of the radiating slug of gas, optical magnification and optical losses. As the shock layer is formed over models with precise dimensions, the width of the radiating shock layer is known accurately and the edge effects can be accounted for through optical imaging using the high speed camera and

computational simulations. The other four uncertainties are features of the focussing optical system. Through the use of an in-situ calibration, all of these uncertainties are accounted for as all of the components are calibrated with any imperfections that they may contain. Consequently the emission spectroscopy system uncertainty is limited to the uncertainty of the calibration lamp itself and these values are outlined in Table 4.

Table 4 Relative uncertainty of the calibration lamp [36].

Spectral Range (nm)	Spectral Bandwidth (nm)	Relative Expanded Uncertainty (k=2)
116.0 - 120.4	0.8	14%
120.6 - 122.6	0.8	36%
122.8 - 170.0	0.8	14%
172.0 - 410.0	1.6	7%

IV.   Results

A raw image recorded on the ICCD camera during an experiment is shown in Figure 11 and shows wavelength on the horizontal axis and spatial distribution on the vertical axis. The intensity of the radiation incident on each pixel is recorded in the form of counts. Through the identification of known spectral lines and the measured dispersion of the grating, it is possible to convert the horizontal pixel position to wavelength.

The camera counts are converted to spectral radiance by first subtracting a dark frame, removing background counts produced due to electronic and thermal noise. The conversion to spectral radiance is then carried out using Equation 9 to produce the result presented in Figure 12.

The spatial location was calibrated using an alignment tool with a known aperture, backlit at the location of the model. The orientation of each image is such that the shock front appears towards the top of the image and the model edge towards the bottom. The shock stand off distances for Condition 1 and Condition 2 were measured using the spatial axis of the spectrometer and found to be 5.1±0.3 mm and 5.5±0.3 mm respectively, agreeing well with the predicted values based on simulations and the 2D/3D correlation. A short region of radiation is measured ahead of the shock
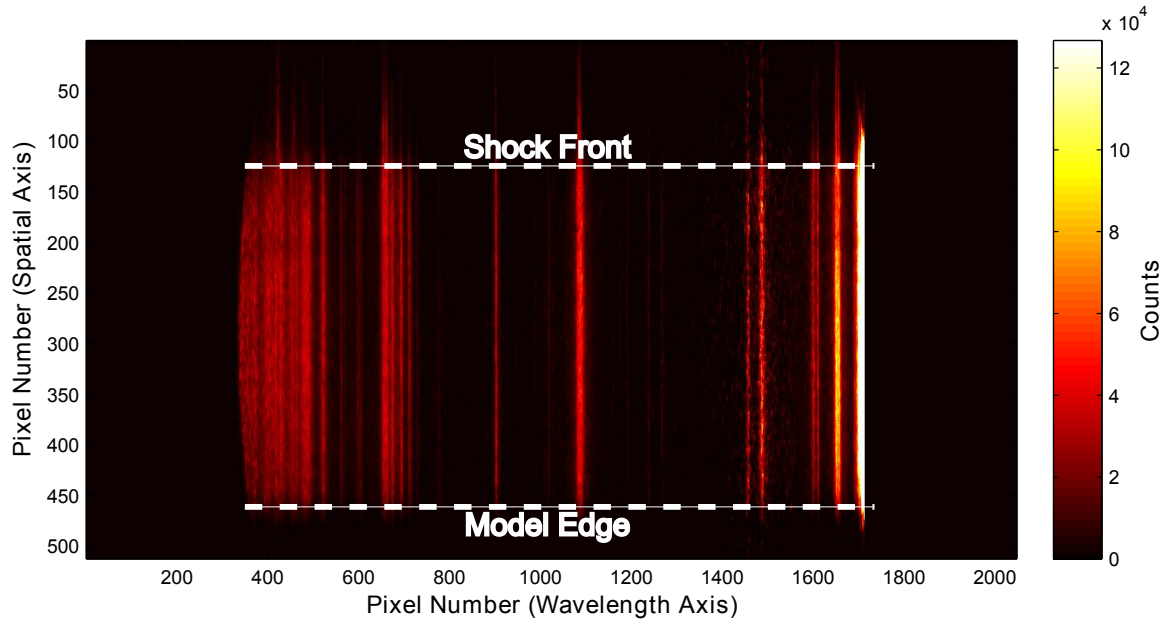
Fig. 11 Raw image acquired on the ICCD observing across the surface of the model at Condition 2.

front. Possible causes for this radiation are precursor radiation, contaminants radiating in the free stream flow and small perturbations of the shock front during the exposure time of ICCD, which was a maximum of $40\,\mu$s.

Integration of the acquired spectral radiance over the full spectral range produces a radiance profile as a function of spatial position along the stagnation streamline, as shown in Figure 12b. This allows for the selection of a spatially uniform emission region over which the spatially resolved spectrum can be averaged to provide a high signal to noise ratio.

The approach outlined was applied to all spectral measurements obtained in the expansion tube and the measured values of through surface and across surface spectral radiance are presented in Figures 15 and 16 for Conditions 1 and 2 respectively.

A. Spectral Line Identification

The National Institute of Standards and Technology spectral line database [38] was used to identify each spectral line, as shown in Figure 13. The dominant radiating particle was found to be atomic nitrogen with small contributions from atomic oxygen and hydrogen. Contaminants found in the spectra obtained include carbon, aluminium and hydrogen. Carbon and iron are repeatedly
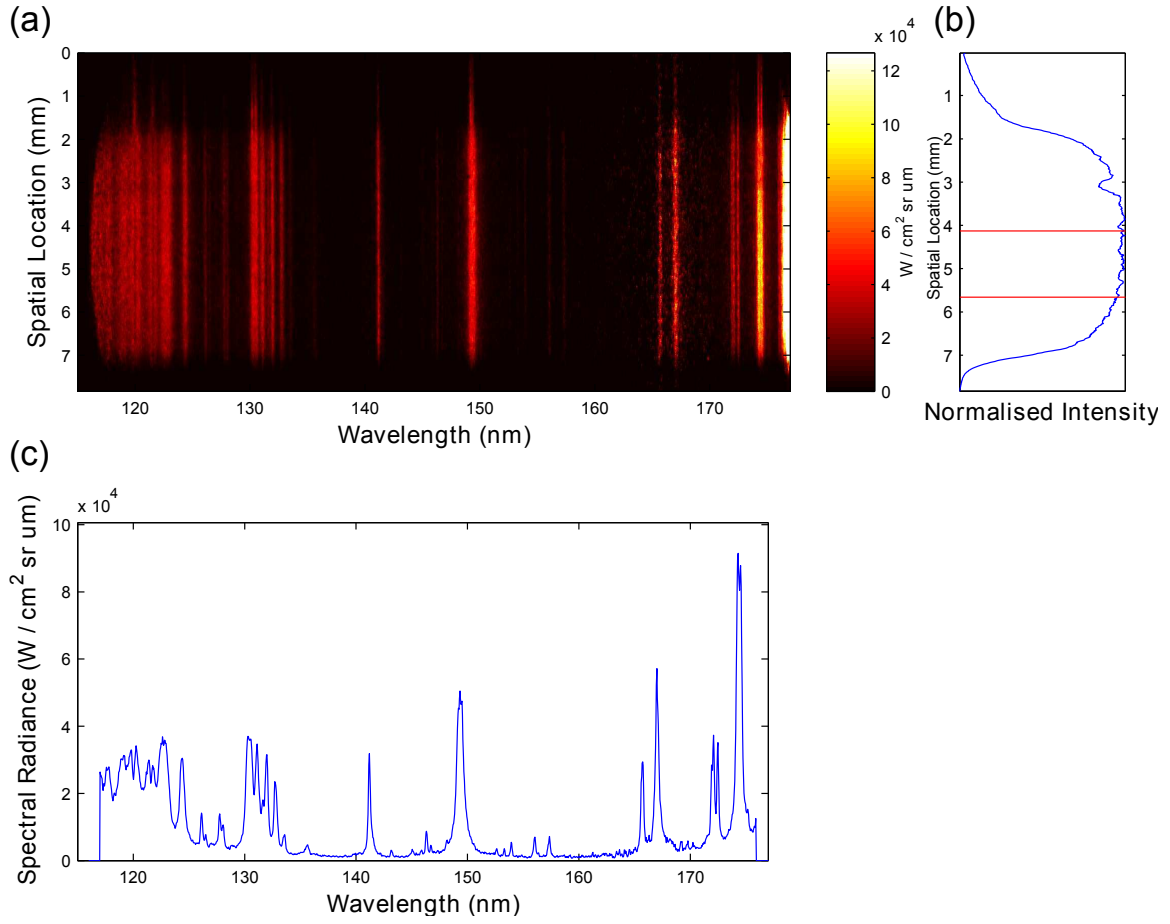
19

Fig. 12 (a) - Calibrated image across observing across the surface at Condition 2. (b) - Spatial distribution of recorded emission and spatial region averaged across. Shock front towards top of image and model surface towards bottom. (c) - Spatially averaged spectrum produced.

observed in spectra and the source is believed to be the walls of the expansion tube. The source of the aluminium contamination is the secondary diaphragm. Small fragments from the secondary diaphragm are able to enter the test gas flow as the diaphragm is positioned downstream of the test gas at the time of firing. Whilst only vaporised aluminium is able to accelerate fast enough to be in the radiating shock layer during test time, the intensity with which it radiates in the VUV makes its spectral lines apparent in the spectrum. Spectral regions containing contaminants were omitted from the remaining analysis but have been retained for future analysis.
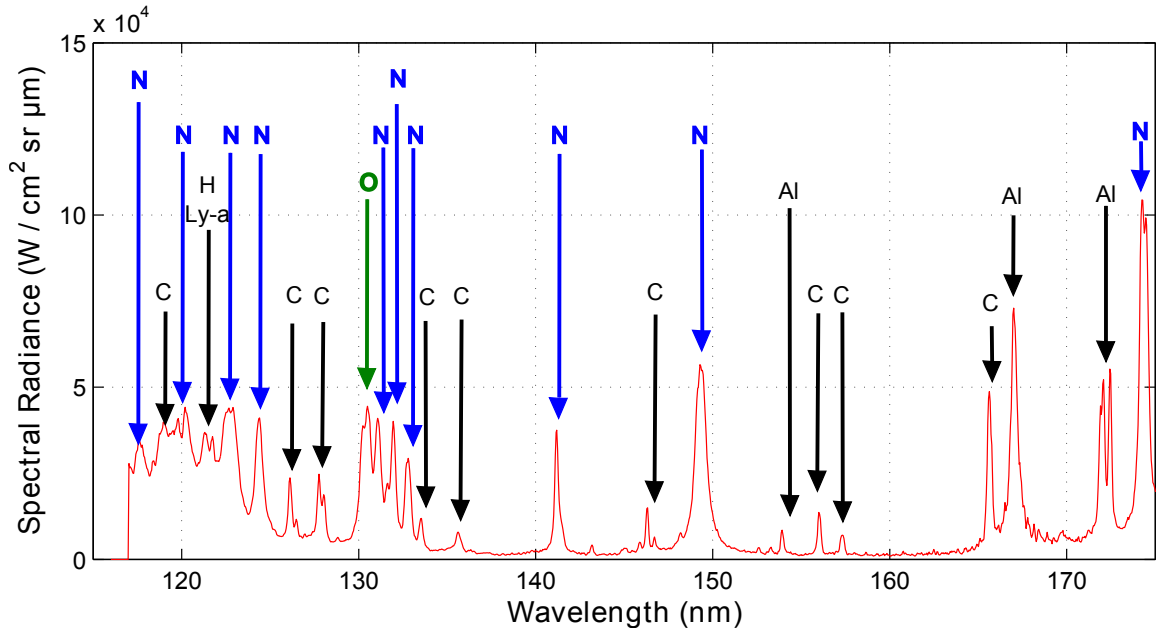
Fig. 13 Chemical species responsible for each spectral line observed.

B. Repeatability Study

A repeatability study was conducted for the across surface optical path at Condition 1. The evacuated light tube was removed for the repeatability study to conserve windows and consequently the optical path was sealed at the edge of the test section. Provided the free stream conditions and test section pressure remained consistent between experiments, the level of absorption between the model and the edge of the test section would remain constant. This absorption was not quantified as it was not required for a measure of system repeatability but could be significant.

Spectral results of the repeatability study, shown in Figure 14, indicate repeatability of the measured spectral radiance to within 15% across the wavelength range for all spectral lines. Integrated values normalised by one of the tests are presented in Table 5 and show a variance in total integrated spectral radiance of 12% from the average.

C. Datasets Produced

Figures 15 and 16 provide the final datasets produced by this study with the regions containing contaminants subtracted from the spectra. Two spectra are provided for each experimental configuration to highlight the repeatability of the measurements.
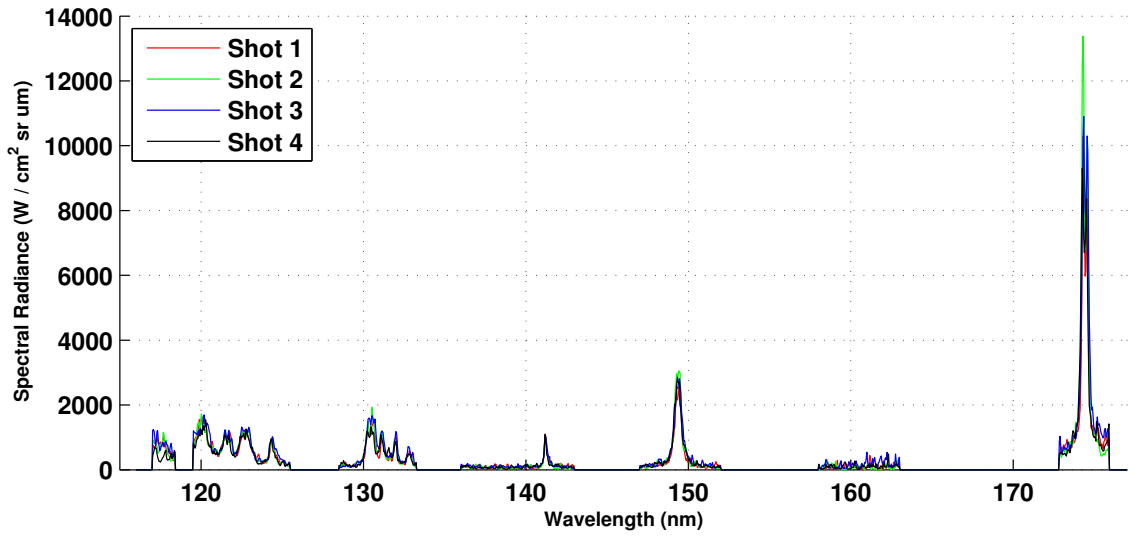
Fig. 14 Results from repeatability study of Condition 1 across the VUV range.

Table 5 Total integrated counts and normalised integrals for Condition 1 when observing across the surface of the model.

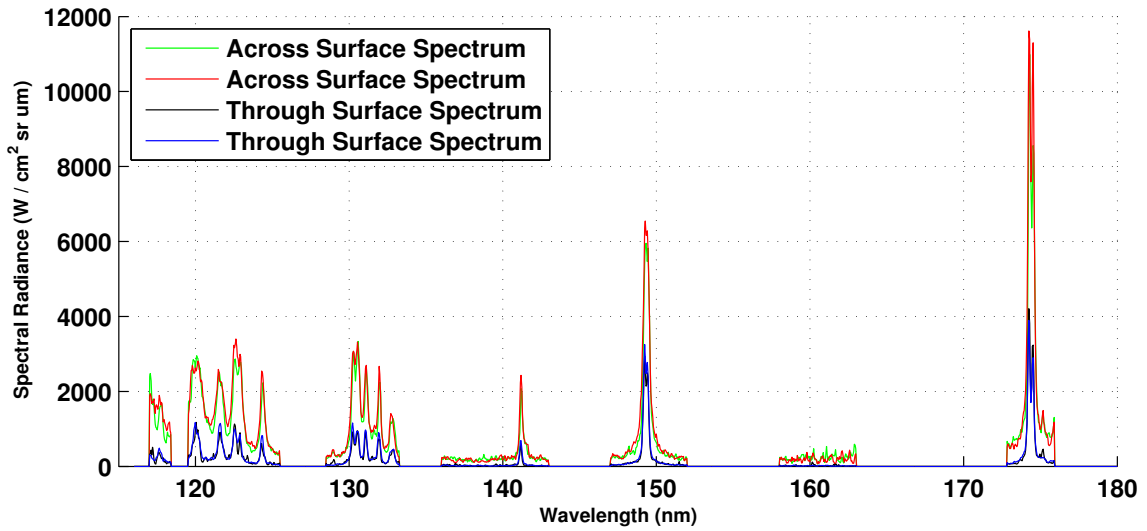| Experiment	Total Integrated Counts (x10^3)	Normalised By the Average
Experiment 1	381	0.95
Experiment 2	408	1.02
Experiment 3	449	1.12
Experiment 4	368	0.92

Fig. 15 Comparison of across surface and through surface spectral measurements at Condition 1. Regions with contaminants set to zero.
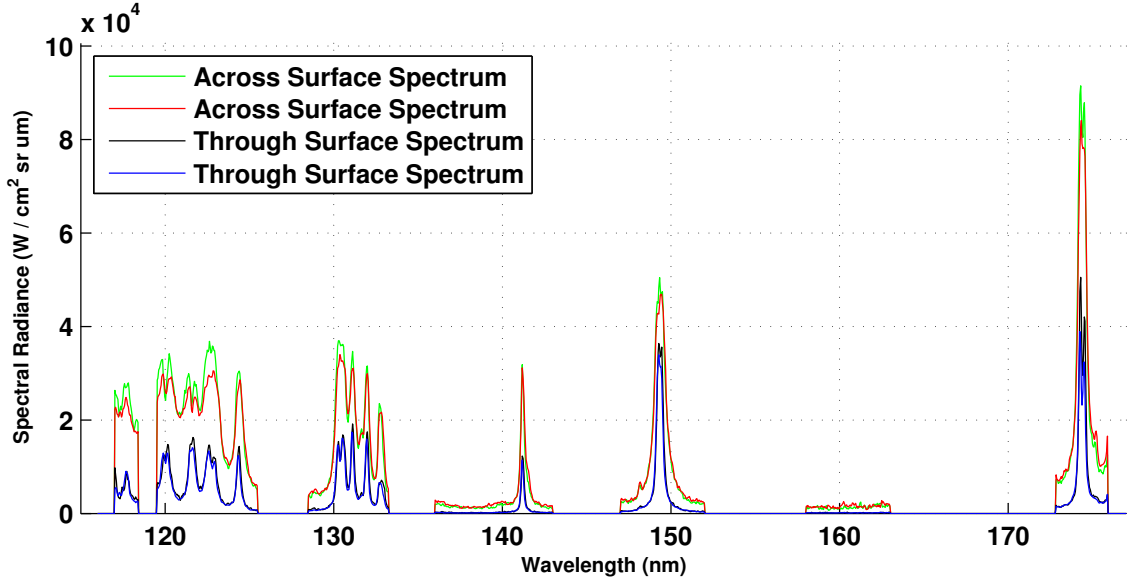
Fig. 16 Comparison of across surface and through surface spectral measurements at Condition 2. Regions with contaminants set to zero.

V. Analysis

The integrals of spectral radiance measured through both optical systems allow for a correlation between radiation observed across the 90 mm model in the uniformly radiating region and the radiation incident on the surface observed through the 5.5 mm shock stand off. Such a correlation provides a test bed for computational analysis and validation of measurements made across shock waves in a shock tube being applied to the design of thermal protection systems. The integrated spectral radiances between 115 nm and 180 nm for both optical paths and conditions are presented in Table 7.

For Condition 1, the intensity of the incident radiation measured was approximately a quarter of that measured in the uniformly radiating region when observing across the shock layer. For the second faster condition, this fraction increased to almost one third. The depth of radiating flow field is 90 mm for across surface measurements and 5.5 mm for the through surface measurements, resulting in a ratio of approximately 0.06. The measured spectral radiance ratios are significantly higher than the ratio of depths of radiating flow fields and this is believed to be due to the strongly self-absorbing nature of VUV radiation.

Table 6 Total VUV radiative heat flux measurements across the surface in the uniformly radiating region and incident on the surface having passed through the boundary layer. Spectral radiance integrated between 115 nm and 180 nm.

	Condition 1	
	Experiment 1	Experiment 2
Across Surface (W/cm^2sr)	28.8±4.0	30.8±4.3
Through Surface (W/cm^2sr)	7.7±1.1	7.2±1.0
Ratio	0.27±0.05	0.23±0.04
	Condition 2	
	Experiment 1	Experiment 2
Across Surface (W/cm^2sr)	400±56	398±56
Through Surface (W/cm^2sr)	116±16	129±18
Ratio	0.29±0.06	0.32±0.07

A.   Equilibrium Computational Analysis

Computational modelling of the equilibrium region observed when viewing across the surface of the model was carried out using the spectral modelling program Specair [39]. The pressure in each simulation was set using the measured pitot pressure values and the gas chemistry was set to equilibrium as calculated by CEA [26]. The depth of radiating flow field for these simulations was set to 90 mm for the across surface comparisons and 5.5 mm for the through surface comparisons. The temperature was selected based on the best fit with measured spectra. Using this approach the equilibrium temperatures were found to be 9,900 K and 12,400 K for Conditions 1 and 2 respectively. The comparison of computed and measured spectra are presented in Figures 17 and 18.

The computed and measured spectra show very good agreement across the spectral range. The only notable discrepancy is the hydrogen Lyman-alpha peak at 122 nm and this is due to the spectral modelling code not including hydrogen emission. The excellent agreement indicates that there is no attenuation of the measured signal by oxygen or water vapour in the optical path.

A similar approach was applied in the computation of through surface spectra with the depth of radiating flow field set to the shock stand off distance. It is currently not possible to set slabs
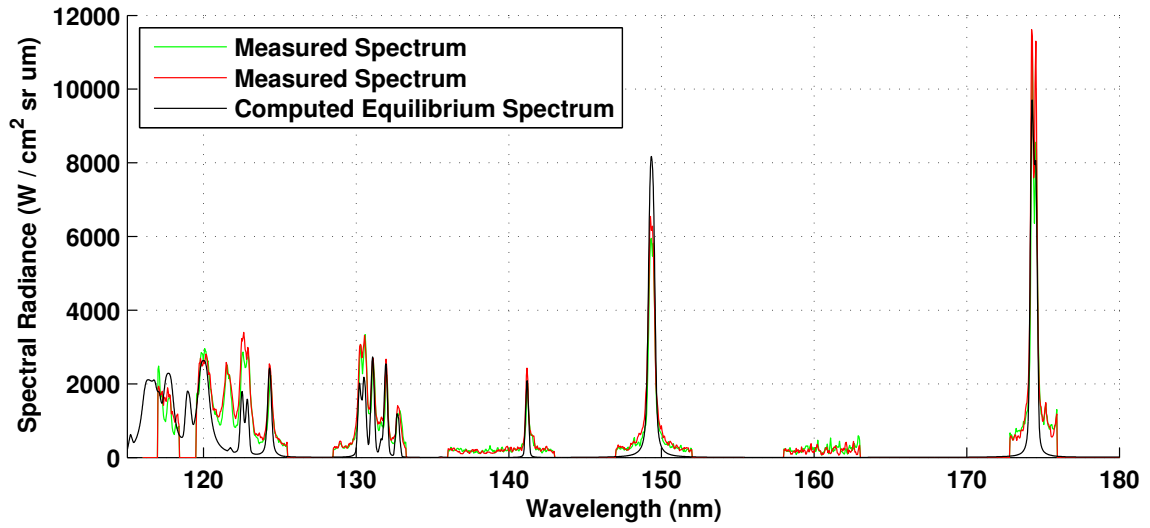
24

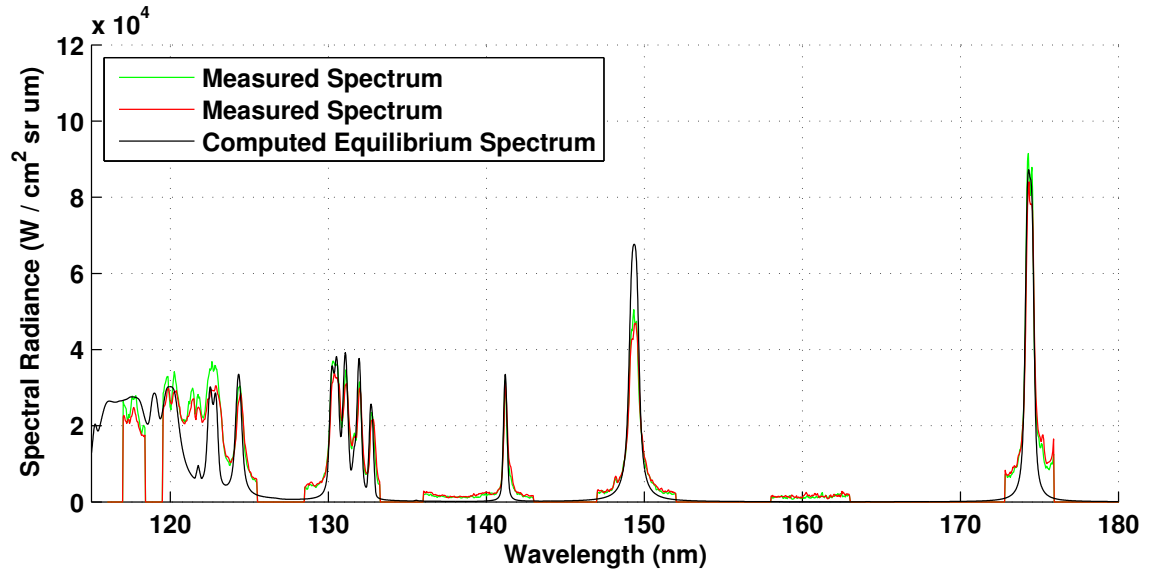Fig. 17 Measured and computed spectra for the across surface viewing direction at Condition 1.

Fig. 18 Measured and computed spectra for the across surface viewing direction at Condition 2.

of varying properties in Specair and therefore the entire shock stand off was assumed to be in thermochemical equilibrium at the same conditions as the across surface computations. The results of this simulation are presented in Figures 19 and 20.
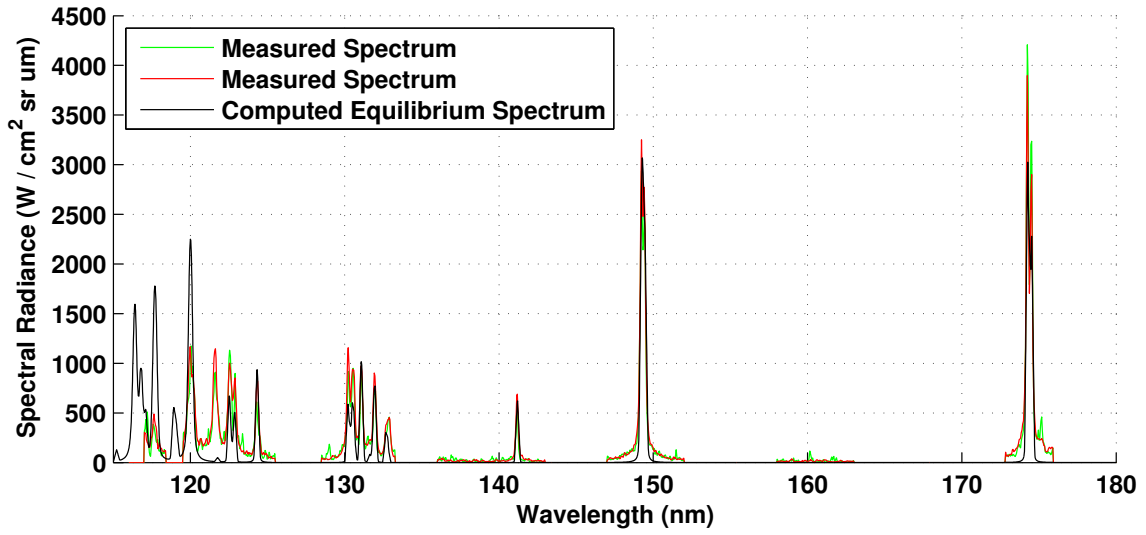
Fig. 19 Measured and computed spectra for the through surface viewing direction at Condition 1.
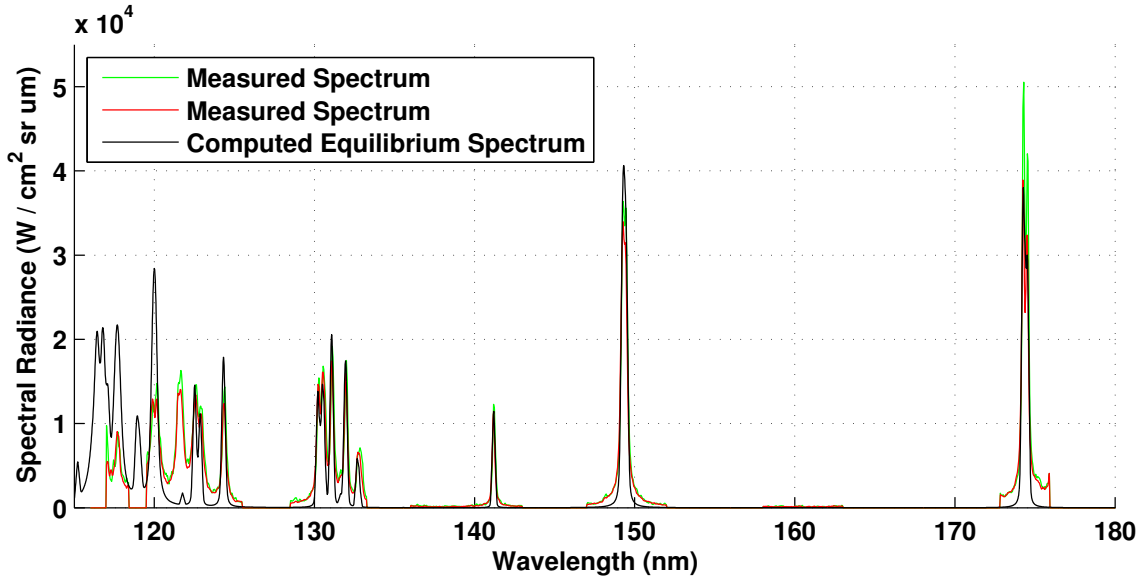

Fig. 20 Measured and computed spectra for the through surface viewing direction at Condition 2.

The computed spectra showed good agreement with the measured values down to 124 nm. Below 124 nm there are discrepancies at the hydrogen Lyman-alpha line as discussed earlier and three atomic nitrogen lines. The discrepancy in the atomic nitrogen lines is believed to be a result of assuming the entire shock layer is in thermochemical equilibrium. Future modelling of the spectrum coupled with computational simulations providing non-equilibrium temperatures and gas chemistry

will be used to investigate this discrepancy. The computed spectral radiance values are also shown to be in very good agreement with the measured values and are detailed in Table 7.

Table 7 Total VUV radiative heat flux measurements and computed values for across the surface in the uniformly radiating region and incident on the surface. Spectral radiance integrated between 115 nm and 180 nm.

Condition 1

	Experiment 1	Experiment 2	Computed
Across Surface (W/cm^2sr)	28.8±4.0	30.8±4.3	26.0
Through Surface (W/cm^2sr)	7.7±1.1	7.2±1.0	7.3
Ratio	0.27±0.05	0.23±0.04	0.28

Condition 2

	Experiment 1	Experiment 2	Computed
Across Surface (W/cm^2sr)	400±56	398±56	449
Through Surface (W/cm^2sr)	116±16	129±18	138
Ratio	0.29±0.06	0.32±0.07	0.31

1. Simulated Spectrum Sensitivity to Temperature

The sensitivity of the simulated spectrum enables a measure of the accuracy of the computed equilibrium temperature. Simulations were carried out at temperature differences of 500 K, 200 K and 100 K to the equilibrium temperature matched with experimental results. The gas chemistry and pressure were kept constant at the matched equilibrium spectra values. The results for Condition 1 and 2 are presented in Figures 21 and 22.

It is apparent that the VUV spectra computed are highly sensitive to temperature across the entire measurement range. Spectral line peak intensities at 149 nm and 174 nm were compared and normalised at the value that matched best with experiments, as shown in Table 8. A change in temperature of 500 K at Condition 1 reduces the intensity by approximately 40% for both spectral lines and a change as small as 100 K produces an intensity variation of 10%. It can be estimated that the measured spectrum can be used to accurately infer the temperature of the radiating shock
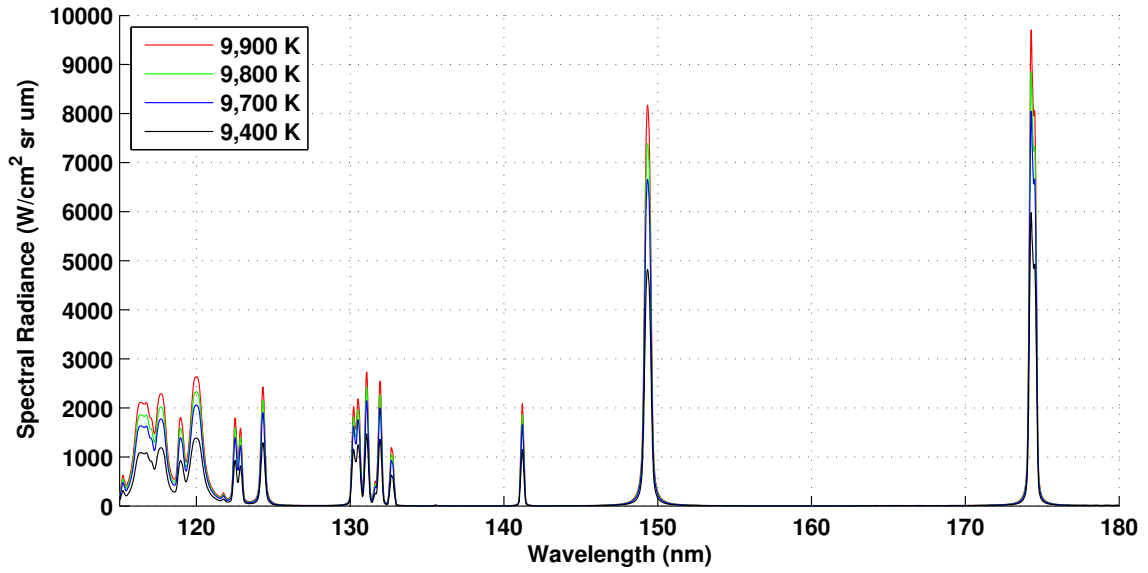
Fig. 21 Air radiation emission at varying temperatures through a 90 mm line of sight. Temperatures simulated are 9,800 K, 9,700 K and 9,400 K to compare with the value determined for Condition 1 of 9,900 K.
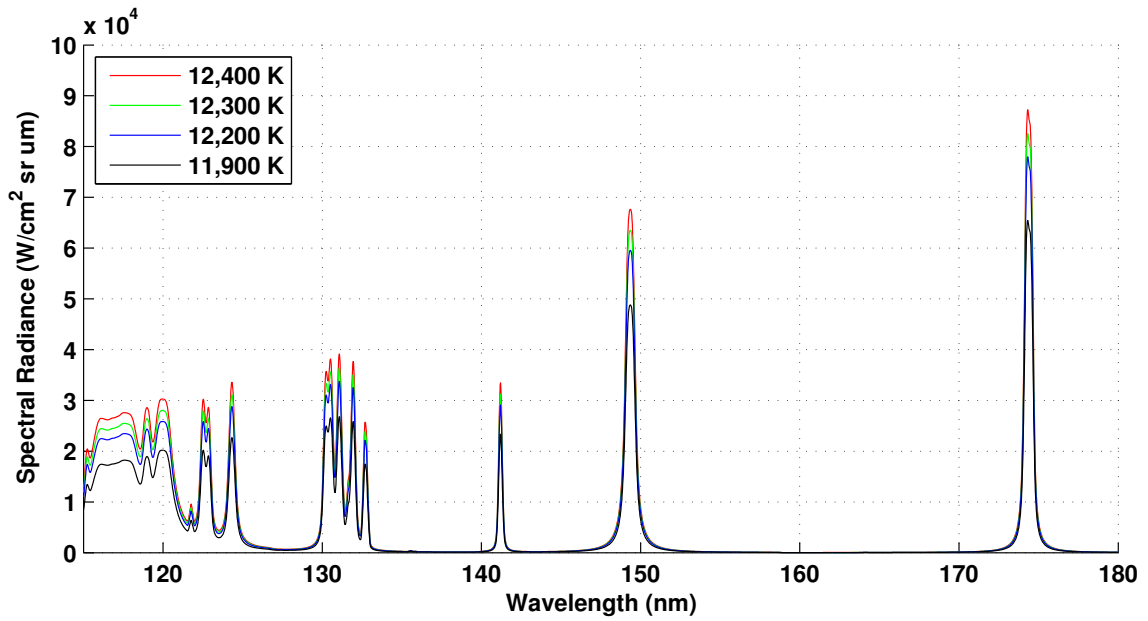

Fig. 22 Air radiation emission at varying temperatures through a 90 mm line of sight. Temperatures simulated are 11,900 K, 12,200 K and 12,300 K to compare with the value determined for Condition 2 of 12,400 K.

layer to within $\pm 200\,\mathrm{K}$, or 2% at $9{,}900\,\mathrm{K}$.

There was lower variation observed in the intensity with respect to temperature of the two spectral lines compared at Condition 2. A $500\,\mathrm{K}$ variation produced a 25-28% change in spectral line intensity and a $100\,\mathrm{K}$ change produced only a 5-6%. These variations are much lower than those calculated for Condition 1 and show that the higher temperature gas spectra is less sensitive to temperature. Based on these calculations, it can be approximated that a change in temperature of $300\,\mathrm{K}$ will produce a variation of less than 15%, and therefore it is estimated that the accuracy of the inferred shock layer temperature at Condition 2 is 2.5%.

Table 8 Simulated intensities for 149 nm and 174 nm spectral lines at a range of temperatures comparable to Conditions 1 and 2 stagnation conditions.

Temperature (K)	149 nm Line		174 nm Line	
	Spectral Radiance $(\mathrm{W}/cm^2\mathrm{sr})$	Normalised at maximum temperature	Spectral Radiance $(\mathrm{W}/cm^2\mathrm{sr})$	Normalised at maximum temperature
Condition 1				
9,400	4,820	0.59	5,980	0.62
9,700	6,600	0.82	8,050	0.83
9,800	7,390	0.90	8,850	0.91
9,900	8,170	1.00	9,710	1.00
Condition 2				
11,900	48,800	0.72	65,500	0.73
12,200	59,600	0.88	78,000	0.80
12,300	63,500	0.94	82,500	0.94
12,400	67,700	1.00	87,200	1.00

VI.   Conclusions

This study has produced calibrated measurements in the VUV spectral range across and through the surface of a flat model at two conditions representative of re-entry flows in the X2 expansion tube. This study has outlined an approach that can be employed to overcome the challenges of measuring spectral data in the VUV. The system produced has shown repeatability to be within

15% for spectral line emission and 12% for integrated spectral intensity. The integrated variation between experiments dropped to below 10% with addition of an evacuated light tube to remove a potentially variable amount of signal absorption in the test section.

The incident radiances measured between 115 nm and 180 nm were $7.5\pm1.0\,\mathrm{W}/cm^2\mathrm{sr}$ for the 10.0 km/s flight equivalent velocity condition and $123\pm17\,\mathrm{W}/cm^2\mathrm{sr}$ for the 12.2 km/s flight equivalent velocity condition. Simulations at equilibrium gas composition were conducted using the spectral modelling program Specair. The simulations provided excellent agreement for across surface spectral measurements and good agreement for the through surface spectral measurements. There were discrepancies in all comparisons at the 122 nm hydrogen Lyman-alpha line and this was due to hydrogen not being included in the spectral modelling. The through surface viewing direction comparison also resulted in discrepancies at wavelengths below 124 nm and these were attributed to the assumption that the entire shock layer is in equilibrium for computational purposes.

References

[1] Kleb, B. and Johnston, C., "Uncertainty Analysis of Air Radiation for Lunar Return Shock Layers," *AIAA Atmospheric Flight Mechanics Conference and Exhibit*, AIAA, Honolulu Hawaii, 2008.

[2] Grinstead, J. H., Wilder, M. C., Olejniczak, J., Bogdanoff, D. W., Allen, G. A., Dang, K., and Forrest, M. J., "Shock-heated Air Radiation Measurements at Lunar Return Conditions," *46th AIAA Aerospace Sciences Meeting and Exhibit.*, AIAA, Reno, NV, 2008.

[3] Palumbo, G., Craig, R. A., Whiting, E. W., and Park, C., "Measured Specific Intensity From 130 to 900 nm At The Stagnation Point Of A Model in An ARCJET Flow Of 7.8 km/sec," *Journal of Quantitative Spectroscopy and Radiative Transfer*, Vol. 57, No. 2, 1997, pp. 207–236.

[4] Sharma, S. P. and Park, C., "Operating characteristics of a 60-and 10-cm electric arc-driven shock tube. I-The driver. II-The driven section," *Journal of thermophysics and heat transfer*, Vol. 4, No. 3, 1990, pp. 259–265.

[5] Cruden, B. A., Martinez, R., Grinstead, J. H., and Olejniczak, J., "Simultaneous Vacuum Ultraviolet through Near IR Absolute Radiation Measurement with Spatiotemporal Resolution in an Electric Arc Shock Tube," *AIAA paper*, Vol. 4240, 2009, pp. 2009.

[6] Itoh, K., Ueda, S., Tanno, H., Komuro, T., and Sato, K., "Hypersonic aerothermodynamic and scramjet research using high enthalpy shock tunnel," *Shock Waves*, Vol. 12, No. 2, 2002, pp. 93–98.

[7] Morgan, R. G., McIntyre, T., Buttsworth, D., Jacobs, P. A., Potter, D., Brandis, A., Gollan, R., Jacobs, C., Capra, B., McGilvary, M., and Eichmann, T., "Shock and Expansion Tube Facilities For the Study of Radiating Flows," *Annexe to European Space Agency Contract Report AMOD-VKI-TN-011*, 2008.

[8] Sheikh, U. A., Morgan, R. G., Zander, F., Eichmann, T. N., and McIntrye, T. J., "Vacuum Ultraviolet Emission Spectroscopy System for Superorbital Reentries," *18th AIAA International Space Planes and Hypersonic Systems and Technologies Conference*, Tours, France., 2012.

[9] Sheikh, U. A., Laux, C. O., Morgan, R. G., and McIntyre, T. J., "Through Surface and Across Surface Vacuum Ultraviolet Spectral Measurements in an Expansion Tube," *44th AIAA Thermophysics Conference*, San Diego, California, USA., 2013.

[10] Parker, R., Dufrene, A., MacLean, M., Holden, M., DesJardin, P., Weisberger, J., and Levin, D., "Emission Measurements from High Enthalpy Flow on a Cylinder in the LENS-XX Hypervelocity Expansion Tunnel," 2013.

[11] Balter-Peterson, A., Nichols, F., Mifsud, B., and Love, W., "Arc jet testing in NASA Ames Research Center thermophysics facilities," *AIAA Materials Specialist Conference-Coating Technology for Aerospace Systems*, Vol. 1, 1992.

[12] Caristia, S., De Filippis, F., Del Vecchio, A., and Graps, E., "Scirocco PWT facility for high temperature material assembly testing," *54 th International Astronautical Congress*, 2003.

[13] Louzet, A., Lemal, A., and Laux, C.O "Radiation-Shapes-Thermal Protection Investigations,", Technical Report, 2011.

[14] Bottin, A., Carbonaro, M., Vander Haegen, V., and Paris, S., "Predicted & Measured Capability of the VKI 1. 2 MW Plasmatron Regarding Re-Entry Simulation," *Aerothermodynamics for space vehicles*, Vol. 426, 1999, p. 553.

[15] Fletcher, D.G. and Playez, M., "Characterization of supersonic and subsonic plasma flows," *AIAA Paper*, Vol. 3294, 2006, pp. 2006.

[16] Auweter-Kurtz, M. and Wegmann, T., "Overview of IRS plasma wind tunnel facilities," Tech. rep., DTIC Document, 2000.

[17] Sagnier, P., Verant, J.-L., Devezeaux, D., Mohamed, A.K. and Masson, A., "Flow characterization in the ONERA F4 high-enthalpy wind tunnel," *AIAA journal*, Vol. 36, No. 4, 1998, pp. 522–531.

[18] Sheikh, U. A., Jacobs, C., Laux, C. O., Morgan, R. G., and McIntyre, T. J., "Measurements of High Enthalpy Radiating Flows in the Vacuum Ultraviolet," *29th International Symposium on Shock Waves*, Madison, WI, USA., 2013.

[19] Jacobs, C., Sheikh, U., MacDonald, M., and Laux, C., "Vacuum Ultraviolet Radiation Studies in a Plasma Torch Facility From 170 - 200 nm," *44th AIAA Thermophysics Conference*, AIAA, San Diego, California, USA., 2013.

[20] Ndiaye, A. A. and Lago, V., "Optical spectroscopy investigation of N2–CH4 plasma jets simulating Titan atmospheric entry conditions," *Plasma Sources Science and Technology*, Vol. 20, No. 1, 2011, pp. 015015.

[21] Lago, V., Lebé, A., Dudeck, M., Pellerin, S., Renault, T., and Echegut, P., "Entry conditions in planetary atmospheres: emission spectroscopy of molecular plasma arcjets," *Journal of thermophysics and heat transfer*, Vol. 15, No. 2, 2001, pp. 168–175.

[22] Canning, T. N., Seiff, A., and James, C. S., "Ballistic-range technology," Tech. rep., DTIC Document, 1970.

[23] Gildfind, D., Morgan, R., McGilvray, M., Jacobs, P., Stalker, R., and Eichmann, T., "Free-piston driver optimisation for simulation of high Mach number scramjet flow conditions," *Shock Waves*, Vol. 21, No. 6, 2011, pp. 559–572.

[24] Gildfind, D. E., *Development of High Total Pressure Scramjet Flow Conditions using the X2 Expansion Tube*, Ph.D. thesis, 2012.

[25] James, C., Gildfind, D. E., Morgan, R. G., Jacobs, P. A., and Zander, F., "Designing and Simulating High Enthalpy Expansion Tube Conditions," *Submitted to 2013 Asia-Pacific International Symposium on Aerospace Technology*, Sunport Hall, Takamatsu, Japan, 2013.

[26] McBride, B. J. and Gordon, S., "Computer program for calculating and fitting thermodynamic functions," Tech. rep., NASA Technical Report, RP-1271, 1992.

[27] Eichmann, T. N., McIntyre, T. J., Bishop, A. I., Vakata, S., and Rubinsztein-Dunlop, H., "Three-dimensional effects on line-of-sight visualization measurements of supersonic and hypersonic flow over cylinders," *Shock Waves*, Vol. 16, No. 4-5, 2007, pp. 299–307.

[28] Kurtz, J., Palmer, R., Thomas, A., McIntyre, T., and Steinberg, T., "Bow-shock radiation on model

surfaces in super-orbital flows," *21st International Symposium on Shock Waves*, Keppel Island, Great Barrier Reef, Queensland., 1997.

[29] Crystran, "Magnesium Fluoride Datasheet," Website, November 2013.

[30] Shimadzu, "Private Communication," .

[31] Lu, H. C., Chen, K. K., Chen, H. F., Cheng, B. M., and Ogilvie, J. F., "Absorption cross section of molecular oxygen in the transition E3u-v=0 - X3g -v =0 at 38 K," *Astronomy and Astrophysics*, Vol. 520, 2010, pp. A19.

[32] Pedrotti, F. L., Pedrotti, L. M., and Pedrotti, L. S., *Introduction to Optics*, Addison-Wesley, 3rd ed., 2006.

[33] Roth, A., *Vacuum Technology*, Elsevier, 1990.

[34] Yoshino, K., Freeman, D. E., Esmond, J. R., and Parkinson, W. H., "High resolution absorption cross section measurements and band oscillator strengths of the (1, 0)-(12, 0) Schumann-Runge bands of O_2," *Planetary and Space Science*, Vol. 31, No. 3, 1983, pp. 339–353.

[35] Mota, R., Parafita, R., Giuliani, A., Hubin-Franskin, M.-J., Lourenco, J., Garcia, G., Hoffmann, S., Mason, N., Ribeiro, P., Raposo, M., et al., "Water VUV electronic state spectroscopy by synchrotron radiation," *Chemical physics letters*, Vol. 416, No. 1, 2005, pp. 152–159.

[36] Bundesanstalt, P.-T., "Calibration Certificate," 2011.

[37] Brandis, A., "Experimental study and modelling of non-equilibrium radiation during Titan and Martian entry," Ph.D. thesis, School of Mechanical and Mining Engineering , The University of Queensland, 2009.

[38] Ralchenko, Y., Jou, F. C., Kelleher, D. E., Kramida, A. E., Musgrove, A., Reader, J., Wiese, W. L., and Olsen, K., "NIST atomic spectra database (version 4.0)," *National Institute of Standards and Technology, Gaithersburg, MD*, 2010.

[39] Laux, C.O., Spence T.G., Kruger, C.H., and Zare, R.N., "Optical Diagnostics of Atmospheric Pressure Air Plasmas", *Plasma Sources Science and Technology*, Vol. 12, pp. 125-138, 2003.